Portable Fourier transform infrared spectroradiometer for field measurements of radiance and emissivity

Andrew R. Korb, Peter Dybwad, Winthrop Wadsworth, and John W. Salisbury

A hand-held, battery-powered Fourier transform infrared spectroradiometer weighing 12.5 kg has been developed for the field measurement of spectral radiance from the Earth's surface and atmosphere in the 3–5-μm and 8–14-μm atmospheric windows, with a 6-cm^{-1} spectral resolution. Other versions of this instrument measure spectral radiance between 0.4 and 20 μm, using different optical materials and detectors, with maximum spectral resolutions of 1 cm^{-1}. The instrument tested here has a measured noise-equivalent delta T of 0.01 °C, and it measures surface emissivities, in the field, with an accuracy of 0.02 or better in the 8–14-μm window (depending on atmospheric conditions), and within 0.04 in accessible regions of the 3–5-μm window. The unique, patented design of the interferometer has permitted operation in weather ranging from 0 to 45 °C and 0 to 100% relative humidity, and in vibration-intensive environments such as moving helicopters. The instrument has made field measurements of radiance and emissivity for 3 yr without loss of optical alignment. We describe the design of the instrument and discuss methods used to calibrate spectral radiance and calculate spectral emissivity from radiance measurements. Examples of emissivity spectra are shown for both the 3–5-μm and 8–14-μm atmospheric windows.

Key words: Fourier transform infrared spectroradiometer, portable spectrometer, infrared radiance measurement, radiometric calibration, spectral emissivity calculation.

1. Introduction

A portable, battery-powered Fourier transform infrared (FTIR) spectroradiometer, called the μFTIR, has been developed by Designs and Prototypes for the field measurement of spectral radiance from the Earth's surface and atmosphere. Versions of this instrument with a 6-cm^{-1} spectral resolution have been used by Johns Hopkins University and others[1] to measure radiances in the 3–5-μm and 8–14-μm atmospheric windows. Prototype versions of this instrument have been developed that attain spectral resolutions as high as 1 cm^{-1} and that operate at wavelengths ranging from 0.4 to 20 μm. It is in the infrared, however, that readily portable and highly accurate field spectroradiometers have been needed for a variety of applications for some time (see below), and the μFTIR is the first instrument to meet these requirements fully. The purpose of this paper is to provide the first comprehensive description of this instrument and its operation.

Portable spectrometers were originally developed for the battlefield detection of chemical agents.[2] These instruments have also been used to monitor atmospheric composition, particularly pollution.[3,4] Small FTIR spectrometers have also been developed as spaceborne instruments.[5–7] The use of spectrometers in space has, in turn, spurred a need for measurements of radiance from the ground, i.e., the so-called ground-truth measurements, to verify calibration, provide atmospheric correction data, and to measure the emissivity of terrestrial surface materials that cannot be measured in the laboratory.[1] Spectroradiometers developed for these reasons are now being used in the field to advance the understanding of the emission and propagation of infrared radiation from field samples,[1,8] to verify atmospheric

A. Korb and J. Salisbury are with the Morton K. Blaustein Department of Earth and Planetary Sciences, Johns Hopkins University, North Charles Street, Baltimore, Maryland, 21218. A. Korb is also with Science Systems and Applications, Inc., 5900 Princess Garden Parkway, Suite 300, Lanham, Maryland 20706. P. Dybwad and W. Wadsworth are with Designs and Prototypes, 38 Berkeley Street, Nashua, New Hampshire 03063.

Received 26 June 1995; revised manuscript received 13 October 1995.

0003-6935/96/101679-14$06.00/0

radiation transfer models,[9] and to study ozone-affecting trace gases in the atmosphere,[3] cloud properties,[10] and the greenhouse effect.[11]

The effort to develop portable field spectrometers has concentrated on FTIR spectrometer designs. FTIR spectrometers are preferred because these designs have energy throughput and multiplex advantages that allow wide spectral coverage without sacrificing spectral resolution or signal-to-noise ratio.[12] Bringing FTIR spectrometers into the field, however, has been challenging. One of the challenges has been portability, because size, weight, and power requirements increase the effort and expense needed to bring an instrument into the field. Another difficulty is alignment sensitivity, which limits the use of most interferometers to shock-resistant optical tables. Finally, radiometric calibration of ambient temperature interferometers can be difficult, because the instruments contribute significant radiance to measurements,[13] and because the wide spectral range of the instruments permits observation of sources with brightness temperatures that vary widely with wavelength.

FTIR field instruments have been built by Block and Zachor,[5] Bomem,[10,11,14–16] Brunswick Defense,[2] and Geophysical Environmental Research,[8] among others. The Bomem MR100 series FTIR instrument is perhaps the most commonly encountered field spectrometer. The instrument operates in the 350–6000-cm^{-1} (1.67–28.57-μm) spectral region, with selectable spectral resolutions of 1, 2, 4, 8, 16, 32, 64, or 128 cm^{-1}. The overall interferometer dimensions are 50 cm × 56 cm × 19 cm, excluding the output optics, and the interferometer alone weighs 45 kg (100.8 lb). The system requires approximately 75 W of power and must be protected against wind, dust, and humidity. The weight, power requirements, and relative fragility of the instrument restrict the field use of the Bomem to applications for which the instrument can be transported into the field with a vehicle.

In contrast, the M21 remote sensing chemical agent alarm made by Brunswick Defense[2] is the result of the evolution of instruments designed to detect chemical agents in the battlefield. Delivered in 1991, the M21 is man portable (may be carried by one or more people), weighing 23.6 kg (52 lb) for optics and electronics. The instrument can be mounted on a vehicle, but for measurements the vehicle must be stopped and the spectrometer aligned (from within the vehicle). The M21 is pointed upwind, and it measures thermal emission with a mercury cadmium telluride (HgCdTe) detector. The spectrometer discriminates between chemical agents and harmless clouds or dust by using detection–discrimination algorithms based on change detection of spectral features. Identification of spectral features allows the M21 to report the type of chemical agent encountered, but because the instrument is not calibrated in the field, the M21 does not report the concentration of agents.

The thermal infrared interferometer spectrometer, made by Geophysical Environmental Research and originating from a patented design by Designs and Prototypes, was also man portable, weighing ~27 kg (60 lb). This spectrometer, however, made quantitative radiance measurements, calibrated with measurements of blackbodies of known temperature, between 2.5 and 14 μm with an 8-cm^{-1} resolution. Radiometric calibration was sufficiently accurate to derive emissivities in the laboratory within 0.02 in the 8–14-μm region, once thermal equilibrium was reached. This spectrometer design pioneered the ability to make measurements without the need for optical alignment adjustments, and operation from moving vehicles. Nonetheless, the spectrometer was not easy to operate in the field. Because the instrument lacked temperature control, reaching thermal equilibrium required 3 h in the laboratory. In the field, equilibrium was harder to achieve and measurements were less accurate. In addition, the instrument weight made it difficult to carry.

These limitations were corrected in the μFTIR instrument discussed here, which retained and refined the advantages of the thermal infrared interferometer spectrometer. Built by Designs and Prototypes, the μFTIR is temperature controlled and measures radiances between 3 and 14 μm with higher resolution and better accuracy than its predecessor. The μFTIR, moreover, is hand portable (may be carried with one hand), as described in Section 2.

2. Instrument Design

A. Optical Design

The μFTIR optics were designed by one of the authors (P. Dybwad of Designs and Prototypes) for portable spectroradiometer instruments and for use embedded within manufacturing processes and other laboratory instruments. The design utilizes the high-throughput advantage of the Michelson interferometer spectrometer to build the smallest and lightest FTIR instrument to fill an infrared detector field of view. The design can attain a spectral resolution of 1 cm^{-1}, with data points every 0.5 cm^{-1}, but the design criteria for the instrument tested called for a resolution of 6 cm^{-1}. Measurements of water vapor lines near 8 μm confirm that the full width at half-maximum resolution is 3 cm^{-1}.

Reducing the size of such an instrument from desktop to coffee mug dimensions was accomplished through innovations in optical design and accessory component selection. The entire interferometer cavity is made from two KBr prisms, separated by a minute air gap, which together form a hexagon, shown in Fig. 1(a). Instead of the use of component mirrors and a beam splitter, optical coatings are applied to the prisms. This permits omission of the bulk of the mounts for optical components, as well as structure to support components to optical tolerances. The much denser packaging results in a short optical

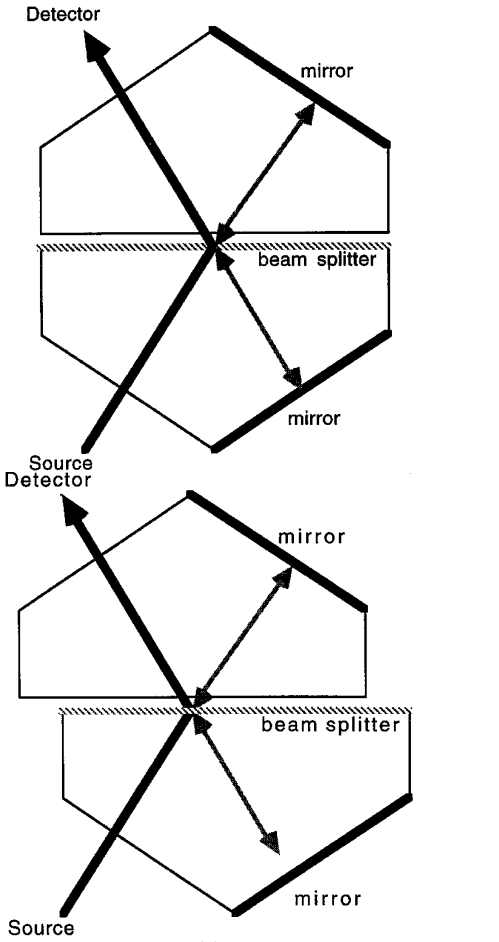

Fig. 1. (a) Schematic of the μFTIR interferometer showing the path difference achieved by the offset of one of the KBr prisms by distance S (in centimeters). In practice, both prisms are offset by distance S in opposite directions to increase the path length difference. The resolution of the interferometer (in inverse centimeters) is $1/4Sn \sin(\theta)$, where n is the index of refraction of KBr and θ is the angle between the direction of motion and the mirrored sides of the prisms. (b) Diagram showing the μFTIR optical module. The thermoelectric enclosure is indicated by the dashed lines; MCT, mercury cadmium telluride.

beam path and greatly reduced growth of the field of view through the instrument. Beam growth is further reduced in comparison with the conventional air-filled Michelson design by the refractive index (1.5) of the KBr material. Overall, these advantages amount to a factor of 2 reduction in equivalent throughput aperture, and a reduction in size and weight of the optical cavity by a factor of 8 compared with the smallest possible conventional air-filled Michelson design.

As a way to take advantage of the optical compactness, an interferometer drive was devised to match the scale of the instrument without sacrificing the accuracy. The drive is mass balanced, resulting in high tolerance to tilt, motion, and vibration (see Subsection 4.F). The drive motor consumes approximately 1 W of power. A small laser diode, optically stabilized at 0.780 μm, replaces the usual helium–neon tube source of the reference interferometer. The reference interferometer provides reference signals for the servo and sampling electronics through a separate optical channel in the interferometer. The interferometer, shown in Fig. 1(b), is sealed on the input and output side by ZnSe lenses that retain a N_2 gas purge and allow a straight optical path from the foreoptics to the detector. The complete interferometer weighs just 800 g.

The foreoptics collect light into the interferometer with an interchangeable, off-axis parabolic mirror mounted on a swivel head, aimed by through-the-lens optics. Current foreoptic systems consist of 2.5-cm-diameter $F12$ or 5-cm-diameter $F25$ mirrors, with visible focus ranging from 1 m to infinity. On the output side is a liquid-nitrogen-cooled, two-element detector (HgCdTe and InSb) in a Dewar with a 10-h hold time. Measurements are collected with the HgCdTe detector in the 8–14-μm atmospheric window, and with the InSb detector in the 3–5-μm window. The detector is selected with a switch on the optical housing. Preamps for each detector are mounted on the Dewar.

The dimensions, weight, and average power requirements of system components are listed in Table 1. Total system weight (including optics, electronics in the attaché case, and computer) is 12.5 kg. A battery to supply 4 h of system power adds another 2.5 kg.

Table 1. Instrument Components Listed with Weight, Dimensions, and the Time-Averaged Power Requirements

Component	Weight (kg)	Dimensions (cm)	Time-Averaged Power Requirement (W)
Interferometer	0.8	9 (diam.) × 15	1
Optics thermal enclosure	3.6	25 × 25 × 20	10
Computer	2.7	22 × 28 × 5	Independently powered
Electronics, in attaché case	4.85	33 × 46 × 5	6
Blackbody	0.45	6 (diam.) × 8	1
Total	12.4 kg	33 × 46 × 32	18 W (1.5 A at 12 V dc)

B. Electronics

The optical head is connected with a single 5-m cable to the attaché case containing the instrument electronics. The top of the case is used as a sunshade for the computer. The electronic boards are mounted underneath a panel in the bottom of the case. The computer, temperature-controlled blackbody, temperature readouts, system controls, and indicators are mounted on top of the panel. Power for the system is 12-V dc, drawn through a power cord that connects to a car cigarette lighter, system batteries, or to an ac supply that accepts power from any outlet worldwide, and that serves as the battery charger for the system batteries.

The optical head is temperature controlled by a thermoelectric enclosure that maintains a relatively constant instrument temperature. Thermal control improves instrument calibration accuracy, and it keeps the reference laser diode within a 10 °C operating range in which the laser wavelength is constant. There are two set point temperatures, i.e., one close to 20 °C, the other close to 30 °C, that are selected with a switch to conserve battery power in different climates.

The blackbody used for calibrating the measurements is also temperature controlled. The stabilized blackbody temperature can be set to one of 12 temperatures, from 10 to 65 °C in 5-deg increments. The controller is a switching type, for high efficiency and longer battery life, that can heat or cool the blackbody. The temperature stability is ± 0.1 °C. The blackbody has a ribbed surface coated with a porous infrared black coating that has a high emissivity in the infrared. A thermoelectric cooler attached behind the blackbody surface pumps heat in or out of the blackbody surface to an ambient heat sink fan. A 100-Ω platinum resistive thermometer senses the temperature, which is displayed on the control panel. The instrument temperature, measured by another platinum resistive thermometer mounted on the IR-blackened aperture stop, is displayed here as well. These thermometers are traceable to the National Institute of Standards and Technology for accuracy.

The servo board that controls the interferometer drive takes its input from the reference interferometer. There are also two optical limit switches on the scan motor to sense the ends of the scan. A classic, linear proportional plus integral control loop drives the scan motor to maintain the frequency of the laser sine wave (and thus scan speed) at its set point. Damping is done mechanically, resulting in no distinct resonant frequencies. An *H*-bridge power amplifier drives the motor in both directions using a single voltage supply.

The sampling board powers the IR detector and receives IR detector signals, using the laser reference channel for sampling. In this way, any speed fluctuations in the servo are tracked, and the wavelength resolution and accuracy are maintained. The IR signal is first passed through an antialias filter, which is designed for constant group delay versus frequency. The filtered IR signal is then sampled by a 16-bit analog-to-digital converter. A low-noise dc–dc converter supplies positive and negative power to both the detector and sampling channel.

The output from the analog-to-digital converter is a serial data stream, a clock, and a gate signal. These are combined with a digital turnaround signal from the servo board and passed to a digital signal processor (DSP) board. The board is a PC bus type based on the AT&T DSP32C floating point processor, connected to the external expansion connector of the system PC. The DSP performs the fast Fourier transform on the incoming data stream in real time, coadding spectra rather than interferograms. Data are acquired by the DSP in the background into one of two memory buffers, using direct memory access on its high-speed serial input. An interrupt is generated at each scan turnaround. This causes the DSP to switch input buffers and then process the most recent scan. DSP processing includes finding the center of the symmetric interferogram (the center burst or zero-path-difference point), apodizing the interferogram with a Hanning apodization function, and performing the fast Fourier transform. The native wavelength scale of the instrument is corrected for spectral dispersion in the scanning prisms (using a logarithmic function, so the resulting wavelength scale is nonlinear), and the result is coadded to the average and stored in another buffer. After data acquisition is complete, the final spectrum is uploaded to the computer for processing and storage.

Processing and storage are accomplished by the system software, running on a notebook PC that uses the DOS operating system, controlled with pop-up menus activated by mouse or keypad operations. The software displays each interferogram and the current coadded average spectrum on the PC screen. The coadd can be stopped or reset if an interferogram or spectrum looks defective. Data are processed by selection of a sequence of sample, downwelling, warm blackbody, and cold blackbody measurements. Sample and downwelling sky radiances are calibrated, and then sample emissivities are calculated, in a series of interactive steps completed when radiance and emissivity spectra are saved. A processing function that computes a spectral ratio is also provided to calculate transmittance, reflectance, and absorbance. Data processing is discussed in greater detail in Section 3. The software also performs utilities such as printing, plotting, displaying data files, and exporting data in ASCII form.

3. Data Acquisition and Analysis

A. Instrument Function

The instrument converts infrared spectral radiance measured at the instrument, $L_{S,\,\mathrm{meas}}(\lambda)$, to an output

spectral voltage, $V_S(\lambda)$,[17]

$$V_S(\lambda) = |r(\lambda)L_{S,\,\mathrm{meas}}(\lambda) - r(\lambda)L^{\circ}(\lambda, T_{\mathrm{inst}})|, \qquad (1)$$

where $r(\lambda)$ is the linear instrument responsivity and $L^{\circ}(\lambda, T_{\mathrm{inst}})$ is the complex instrument self-emission. Fences indicate that the instrument output represents the magnitude of the instrument response. Measurements of blackbody calibration sources at two known temperatures permit the calculation of the responsivity and self-emission. Calibration processing then removes these instrument artifacts from the measurement, returning the radiance from the sample as measured at the instrument, $L_{S,\,\mathrm{meas}}(\lambda)$.

The radiance at the instrument differs from the radiance exiting the sample, L_S, because of atmospheric attenuation. The atmosphere between the sample and instrument absorbs and emits sufficient radiation to affect emissivity calculations at distances of more than 1 m in both the 3–5-μm and the 8–14-μm atmospheric windows. The amount of absorption and emission varies with atmospheric water vapor concentration and the distance from the sample to the instrument. The sample and atmospheric temperatures, T_S and T_{atm}, determine the balance between emission and absorption. For the effects of the atmosphere to be decreased, samples are measured over the shortest distances possible. Sample radiance is then assumed to equal the calibrated sample measurement.

Radiance exiting the sample at any wavelength has complementary emitted and reflected components. The directional emissivity $\epsilon_S(\lambda)$ and hemispherical directional reflectance $R(\lambda)$ add to one according to Kirchhoff's law,

$$\epsilon_S(\lambda) = 1 - R_S(\lambda). \qquad (2)$$

The sample radiance can then be expressed as

$$L_S(\lambda) = \epsilon_S(\lambda)B(\lambda, T_S) + [1 - \epsilon_S(\lambda)]L_{\mathrm{DWR}}(\lambda), \qquad (3)$$

where the first term on the right is the self-emission of the sample, at temperature T_S, and $L_{\mathrm{DWR}}(\lambda)$ is the downwelling radiance (DWR) reflected from the sample into the spectrometer with reflectance $[1 - \epsilon_S(\lambda)]$. DWR is the sum of the emission from the atmosphere and solid surfaces in the hemispherical field of view of the sample.

B. Measurement Procedure

The optical head is temperature controlled to increase the calibration accuracy of the instrument, because instrument self-emission varies strongly with instrument temperature. Maintaining instrument temperature constant within 0.1 °C between calibration measurements limits the fractional calibration error from this variability to less than 0.002. In the field, an aluminized heat shield covers the instrument to reduce the solar heat load, but the instrument temperature still tends to rise by 1 or 2 °C through the day in hot, desert environments. For the temperature rise to be minimized while measurements are recorded, the temperature enclosure is activated 1 h before measurements are recorded, while the scan motor is run for 15 min, to allow the optical head to reach thermal equilibrium.

Radiance spectra are recorded when enough scans are coadded to yield an adequate signal-to-noise ratio. The length of integration time is limited because the instrument temperature controller switches off automatically during data collection, to minimize electrical and mechanical interference, thereby allowing the instrument temperature to change. After each measurement the scan motor is turned off, and the controller switches on to reequilibrate the instrument. The optimum length of the on–off duty cycle is a compromise between increased integration time and decreased calibration accuracy. Results shown below were obtained when 16 1-s scans were coadded and then 30 s were allowed for the instrument to reequilibrate.

Calibration measurements are made with the blackbody pressed onto the foreoptic housing. Blackbody temperatures are selected to reduce calibration error, with a cold blackbody temperature just below ambient temperature and a warm blackbody at a temperature just above the warmest sample temperature. This selection of blackbody temperatures is demonstrated by Fig. 2, which shows uncalibrated measurements of quartz sand emission bracketed by measurements of blackbodies at 25 °C and 40 °C. The spectra have similar uncalibrated amplitudes despite dissimilar origins, because much of the amplitude in these spectra was emitted by the instrument, the so-called instrument self-emission.

Sample radiances are measured from a distance of less than 1 m, if possible, to reduce atmospheric attenuation. Measurements are made at angles near normal exitance so that emissivity measured in the field may be compared with complementary laboratory measurements of directional hemispherical reflectance. Downwelling radiances are always measured immediately before, or after, the sample

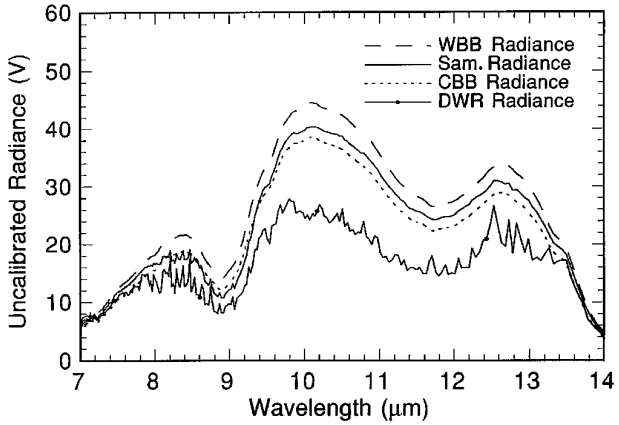

Fig. 2. Uncalibrated instrument radiances of quartz sand, DWR, and blackbody measurements at 25 °C and 40 °C, measured in Florida at an air temperature of 40 °C and at 95% relative humidity, under partly cloudy skies; WBB, warm blackbody; CBB, cold blackbody.

radiance measurement, by collection of the radiance reflected from a diffuse, reflective plate. In the laboratory a Labsphere gold plate is used, whereas in the field, panels made from crinkled aluminum foil taped onto cardboard are frequently used instead, partly because they may be made to any size, and partly because they can be renewed easily after contamination with wind-blown dust. Directional hemispherical measurements of both the gold plate and the crinkled aluminum foil show a reflectance of ~0.94. In either case, the location, orientation, and bidirectional reflectance distribution function (BRDF) of the reflective plate should be identical to those of the sample to measure accurately the DWR reflected by the sample. Although placing the reflective plate on the sample surface satisfies the first two criteria, many natural samples are more diffuse than either the gold plate or crinkled aluminum foil, both of which have a significant specular component. However, this error is small in the 8–14-μm region compared with the error caused by time-dependent variations of DWR. In the 3–5-μm region, where reflected solar radiance can be significant, the BRDF of the sample and reflective plate must be the same, or angles near the angle of specular solar reflection must be avoided.

C. Calibration of Radiance Measurements

The method used to calibrate absolute radiance spectra from uncalibrated instrument measurements is similar to other FTIR calibration methods,[6,7,13,17] with some exceptions motivated by the system requirements for accuracy and simplicity. Phase correction, for example, is not required because all interferograms are double sided. The data processing coadds magnitude spectra, rather than interferograms, to avoid problems associated with aligning interferograms properly, which would require the addition of a white-light interferometer or advanced software development. This coadd averaging uses the magnitude, rather than the real component, of the complex spectra returned by the Fourier transform because magnitude spectra are less affected by slight phase differences between individual spectra, and therefore contribute to a more precise average.

The standard FTIR calibration method assumes that blackbody emissivity is one, and that the instrument responds linearly to an influx of radiance (the error analysis for calibration is discussed in Section 4). The calibration function relating measured data to calibrated radiances at any wavelength is a straight line defined by a slope (responsivity) and y intercept (offset). These two parameters are calculated from uncalibrated magnitude measurements of two blackbodies, V_A and V_H, and the Planck radiances, B_A and B_H, computed from measured blackbody temperatures, T_A and T_H. The responsivity is the conversion efficiency of the instrument, calculated from the ratio of measured and calculated radiances, i.e.,

$$r(\lambda) = \frac{V_H(\lambda) - V_A(\lambda)}{B(T_H, \lambda) - B(T_A, \lambda)}. \quad (4)$$

The offset is the instrument response to radiance from the instrument itself, the instrument self-emission, $L^0(\lambda, T_{\text{inst}})$, which is calculated below:

$$L^0(\lambda, T_{\text{inst}}) = B(T_A, \lambda) - [V_A(\lambda)/r(\lambda)]. \quad (5)$$

Knowledge of the calibration function permits the conversion of uncalibrated instrument radiance $V_S(\lambda)$ to calibrated radiance $L_S(\lambda)$ in standard radiometric units (in this case, watts per square meter per micrometer of spectral range, i.e., $\text{W}/\text{m}^2\ \mu\text{m}$) by dividing by the responsivity, then adding the instrument self-emission:

$$L_S(\lambda) = V_S(\lambda)/r(\lambda) + L^0(\lambda, T_{\text{inst}}). \quad (6)$$

To convert these radiances to units of watts per square meter per steradian per micrometer of spectral range ($\text{W}/\text{m}^2\ \text{sr}\ \mu\text{m}$), divide by pi. Examples of calibrated sample and DWR's are shown in Fig. 3.

D. Downwelling Radiance Correction

The DWR measurement is susceptible to a small error that results from the emission of the diffuse gold plate used for the measurement. If the plate temperature, T_G, exceeds the ambient temperature, then the measured DWR, $L_{\text{DWR, meas}}$, will exceed the actual DWR, L_{DWR}, as shown:

$$L_{\text{DWR, meas}}(\lambda) = L_{\text{DWR}}(\lambda)[1 - \epsilon_G(\lambda)]) + \epsilon_G(\lambda)B(T_G, \lambda), \quad (7)$$

where all the variables are wavelength dependent and ϵ_G is the emissivity of the gold plate, calculated from directional hemispherical reflectance measurements.[18] The error will distort the DWR correction in the emissivity calculation, with maximum errors at sample reflectance maxima, such as the reststrahlen bands of silicates. For the error to be corrected, the gold plate temperature is monitored with a thermocouple during radiance measurements, and the correction is applied later:

$$L_{\text{DWR}}(\lambda) = \frac{L_{\text{DWR, meas}}(\lambda) - \epsilon_G(\lambda)B(T_G, \lambda)}{[1 - \epsilon_G(\lambda)]}. \quad (8)$$

E. Emissivity Calculation

After calibrating the measured sample radiance L_S, using Eq. (6), and finding the corrected DWR's L_{DWR}, one can solve the sample radiance equation above for the spectral emissivity of sample ϵ_S

$$\epsilon_S(\lambda) = \frac{L_S(\lambda) - L_{\text{DWR}}(\lambda)}{B(\lambda, T_S) - L_{\text{DWR}}(\lambda)}, \quad (9)$$

if the sample temperature can be determined.

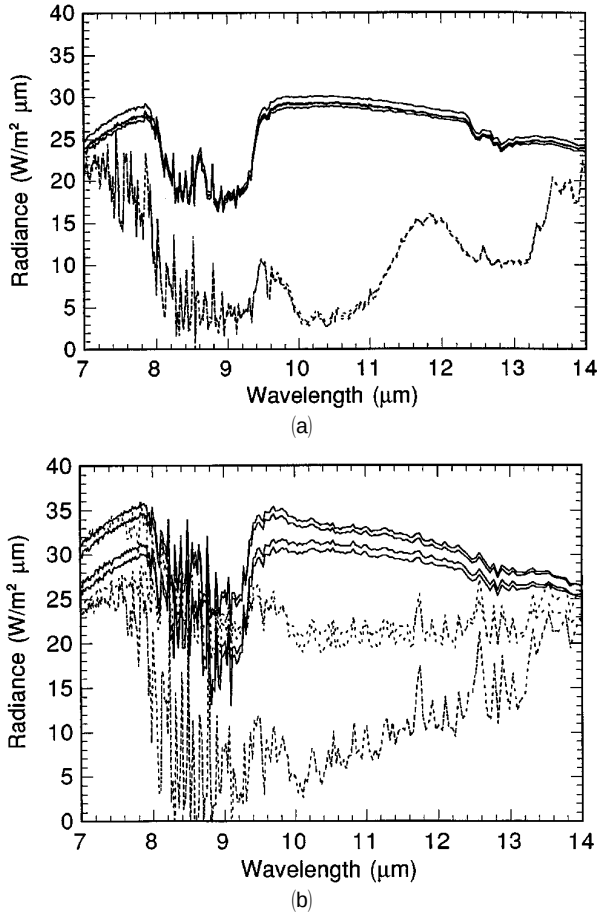

Fig. 3. (a) Calibrated radiances of 75–250 μm quartz sand (solid curves) and DWR's (dashed curves) measured in Nevada at an air temperature of 29 °C and at 9% relative humidity, under clear skies. The DWR spectra were corrected for emission from the diffuse gold plate. The smooth portions of quartz spectra are regions of high emissivity (low reflectance) characterized primarily by the Planck function representing the quartz temperature. The two broad quartz radiance minima between 8 and 9.5 μm are fundamental molecular vibration bands (reststrahlen bands) of quartz combined with reflected DWR emission lines from atmospheric water vapor. The DWR spectra show water vapor line emission features in the 7–9-μm region, the ozone doublet bands near 9.6 μm, and continuum emission with line emission features superimposed from 10 μm to the 14-μm band of CO_2 emission lines. This spectral region contains a calibration artifact caused by the nonlinear response to cold targets that peaks at 11.8 μm (see Subsection 4.D). (b) Four calibrated radiance curves for the same quartz sand measured in Florida at an air temperature of 40 °C and at 95% relative humidity, under partly cloudy skies. The quartz radiances (solid curves) show more structure because of reflection of stronger water vapor line emission features than those in (a). The three DWR spectra (dashed curves) vary considerably as a result of meteorological conditions changing over a time period of 30 min. The calibration artifact from nonlinear response to low-radiance targets is not observed in these spectra, because increased emission from water vapor raises the DWR above the nonlinear threshold.

The sample temperature can be measured directly with a thermocouple, but the measurements must accurately represent the emission temperature because, for example, a 1° temperature change translates to a 2% change in emissivity for a sample with $\epsilon \sim 0.99$ at 32 °C. The low thermal inertia, poor thermal conductivity, and the surface roughness of most natural materials make accurate contact measurements difficult. Man-made materials, particularly metals with high thermal conductivity and smooth surfaces for good thermal contact, are more amenable to direct temperature measurements.

Another technique for finding the sample temperature assumes a maximum sample emissivity (usually 1.0 for a sample of unknown emissivity) at some wavelength within the measured spectral region.[1,19] The μFTIR system software determines the sample temperature graphically by finding the temperature at which a Planck function coincides with the sample radiance. The software substitutes this sample temperature into the emissivity equation to calculate the emissivity at all wavelengths. This method works well in the 8–14-μm atmospheric window for most natural surfaces that have emissivities approaching one at some wavelength in this spectral region.[18] However, some materials, such as carbonates and many man-made materials, do not follow this assumption in the 8–14-μm region. In the 3–5-μm region, where emissivities tend to be lower,[20] the unity emissivity assumption is generally not valid.

For carbonates and man-made materials in the 8–14-μm region, and for most materials in the 3–5-μm region, significantly better emissivity calculations result if the observer has some *a priori* knowledge of the maximum emissivity in the wavelength region. The emissivity spectrum of the particular material does not have to be known; simply knowing the general maximum emissivity of the class of material will make field measurements much more accurate. For example, simply knowing that carbonates have an ϵ_{max} of ~0.95 in the 10–11-μm region will reduce the error of emissivities derived by a factor of ~5 compared with assuming an ϵ_{max} of 1.0. In the 3–5-μm region, where peak emissivities tend to be lower, the use of nonunity peak emissivity will have an even larger effect. Peak emissivities in the 3–5-μm and 8–14-μm regions for many terrestrial materials are provided by Salisbury and D'Aria.[18,20]

If the peak emissivity is known, an iterative procedure may be used to derive the spectral emissivity. One can obtain an initial estimate of sample temperature (and the wavelength of peak emissivity λ_{max}) by fitting the emissivity to one at the wavelength of peak emissivity, following the method described above. One can also calculate the maximum brightness temperature T_{max} (in degrees Kelvin) and the wavelength of maximum brightness temperature λ_{max} directly from the sample radiance spectrum $L_S(\lambda)$ (which, for the μFTIR instrument, is in units of watts per square meter per micrometer) as a function

of wavelength (in micrometers) by using

$$T(\lambda) = \frac{14387.9}{\lambda} \times \frac{1}{\ln(\{3.7418 \times 10^8/[\lambda^5 \times L_S(\lambda)]\} + 1)}. \quad (10)$$

If the emissivity is calculated with temperature T_{max} the emissivity at λ_{max} will be 1.0.

To calculate a nonunity peak emissivity, invert emissivity Eq. (9) to find the Planck function necessary to obtain the expected peak emissivity $\epsilon_{max}(\lambda)$ at λ_{max} with measured sample radiance $L_S(\lambda)$ and corrected DWR $L_{DWR}(\lambda)$:

$$B(\lambda_{max}, T) = \frac{L_S(\lambda) - L_{DWR}(\lambda)}{\epsilon_{max}(\lambda)} + L_{DWR}(\lambda). \quad (11)$$

This value of the Planck radiance at λ_{max} is fed into temperature Eq. (10) to derive a second, better estimate of the sample temperature. The second temperature estimate is used to compute the spectral emissivity with Eq. (9). This spectral emissivity will have a maximum value close to $\epsilon_{max}(\lambda)$ at λ_{max}. If the emissivity maximum is not sufficiently close to $\epsilon_{max}(\lambda)$, then the emissivity is recalculated with Eq. (9), using a temperature perturbed by two or three hundredths of a degree from the second estimate. A best fit of sample temperature at λ_{max} is found by linear interpolation of the sample temperature between this pair of temperatures to the exact extent that $\epsilon_{max}(\lambda)$ interpolates between peak emissivities calculated from this pair of temperatures. Then the emissivity is recalculated for the new temperature estimate. Usually this emissivity matches the expected peak emissivity $\epsilon_{max}(\lambda)$ within 0.1%. Otherwise the temperature is interpolated again, to obtain a better estimate, and the emissivity is recalculated with the new temperature.

These temperature estimates should be fitted at the wavelength of maximum emissivity to reduce the reflected DWR subtracted in the emissivity calculation, because DWR subtraction is usually the largest source of error. At instrument-to-sample distances of a few meters or less, the iterative procedure can be used even on the edge of the atmospheric windows, as is done for quartz, which has an ϵ_{max} of 0.995 at 7.54 μm. As a way to reduce the error caused by fitting the quartz temperature on the narrow atmospheric absorption–emission lines in this region, the wavelength used for temperature fitting is broadened when iterative calculations are made for a few spectral points without any strong absorption features, between 7.48 and 7.62 μm, centered on the wavelength of peak emissivity at 7.54 μm. The goal of this procedure is to find a temperature that sets the emissivity of the group average to the $\epsilon_{max}(\lambda)$ of 0.995 at 7.54 μm. However, if the sample is more than a few meters from the instrument, the iterative temperature fitting of peak emissivity should be shifted to wavelengths with minimal atmospheric absorption, i.e., either 10.2–11.8 μm or 4.5–5.0 μm.

This iterative procedure has been used to calculate emissivities of several materials other than quartz in the 8–14-μm region, including gabbros, diorites, wood (cellulose), various types of live vegetation, bentonite clay, red clay, gravels of several varieties, asphalt, various soils, carbonates, tarps, paints, metal foils, sheets, and vehicles. Similar techniques are also used at the Jet Propulsion Laboratory and the Japanese Geological Survey to calculate emissivity from radiance measurements.[1] The technique has also been applied in the 3–5-μm region to quartz, carbonates, soils, vegetation of various types, paints, metal foils and sheets, tarps, and vehicles. The accuracy in the 3–5-μm region is less precise, as shown below, but the technique described is valid.

One effect that has not been compensated for in this technique is the fact that a rough or particulate surface heated by the Sun may have a distribution of temperatures across its surface, caused by differences in insolation angle or shading. A surface with an inhomogeneous temperature distribution will emit radiation with a mixture of Planck functions, and this mixture will not resemble the Planck function of any single temperature. As a result, the mixture will have a brightness temperature that varies with wavelength, and a process that fits a single temperature at one wavelength will not accurately represent the temperatures at other wavelengths. However, this effect must be small, at least at the relatively high Sun angles experienced in the field, because emissivity calculated from directional hemispherical reflectance and emissivity measured in the field under stable atmospheric conditions are so similar.

F. Wavelength Calibration

The μFTIR instrument has a wavelength dependence that arises from the use of KBr prisms for the interferometer arms. The refractive index of KBr is wavelength dependent, which causes the path length difference to vary with wavelength. The wavelength scales of spectra are automatically adjusted by system software for this dependence on refractive index with a logarithmic correction function. Measurements show that this correction is accurate to within three wave numbers throughout the instrument bandpass.

The accuracy of this wavelength correction is checked before and after field campaigns. The absorption spectrum of polystyrene is measured with the μFTIR instrument and compared with identical measurements made with a Nicolet System 510 with known wavelength calibration.[21] The comparison between the positions of several band centers is used to determine a linear factor to correct measured wavelengths to within 0.03 μm at 10 μm and to within 0.006 μm at 4.5 μm (3 cm^{-1}). This linear correction factor, of the order of 1%, is folded into the setting of the reference laser frequency in the system software, which then automatically corrects the wavelength scale of each measurement.

4. Instrument Performance

A. Signal-to-Noise Ratio

The signal-to-noise ratio provides a measure of the precision of data produced by the system at each wavelength. The signal-to-noise ratio was computed when the uncalibrated radiance from one scan of a 25 °C blackbody was divided by the root mean square (rms) noise measured in the 1.55–2.0-μm region, shown in Fig. 4 for both detectors. These calculations represent the minimum signal-to-noise ratio obtainable because radiance spectra usually coadd 16 scans, corresponding to a signal-to-noise ratio increase by a factor of 4 because of increased integration time. The signal-to-noise spectra demonstrate the instrument passbands between 3–5 and 8–14 μm. These bands are shaped by the wavelength dependence of the optical and electronic components.

B. Noise-Equivalent Temperature Sensitivity

A single, 1-s scan of a blackbody at 25 °C was used to calculate the temperature sensitivity of the instrument. The noise-equivalent delta temperature (NEΔT) was calculated by subtraction of the brightness temperatures calculated for the blackbody radiance and the blackbody radiance after subtraction of the rms instrument noise. The results plotted in Fig. 5 show that the NEΔT is 0.01 K through most of the 8–14-μm window, and less than 0.05 K between 4.5 and 5 μm.

C. Field-of-View Measurements

The correspondence between the visible-light field of view of the aiming optics and the infrared field of view observed by the interferometer was measured to ensure accurate aiming of the instrument. The IR field of view of the instrument was mapped out by measurement of the instrument response to a hot point source as a function of position with respect to the visible field of view.

The measurements, valid for both detectors and both sets of foreoptics, show that the IR field of view is roughly circular and slightly elongated along the long axis of the instrument enclosure, with a small sidelobe on the short axis of the instrument enclosure away from the instrument. This pattern is shown in Fig. 6, which is a contour plot that shows

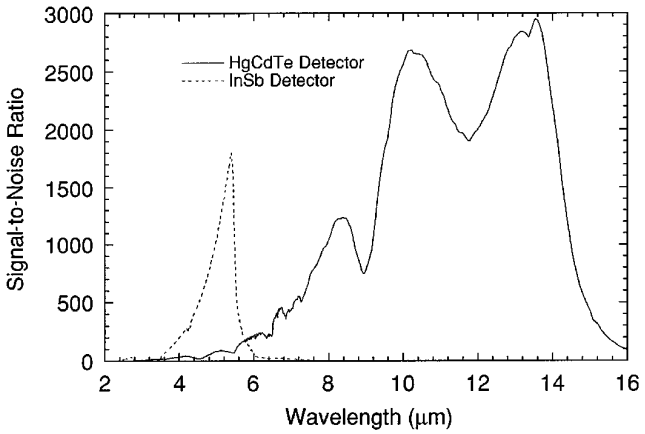

Fig. 4. Spectral signal-to-noise ratio from a single 1-s scan of a 25 °C blackbody for InSb and HgCdTe detectors. The signal-to-noise ratio was calculated when the uncalibrated instrument response to the blackbody at each wavelength was divided by the rms variation of instrument response over 462 spectral points between 1.55 and 2.0 μm, where the variation is only from noise.

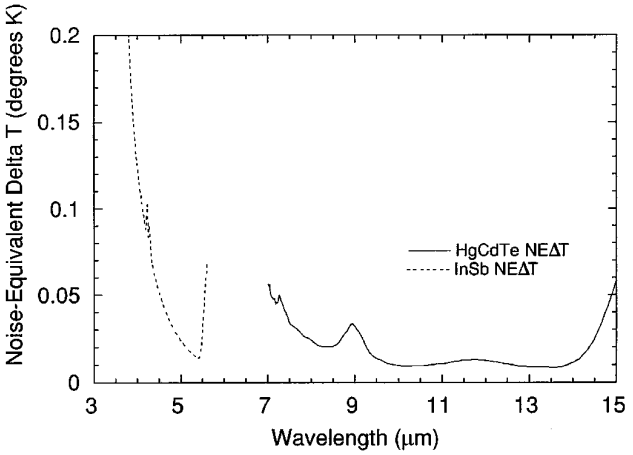

Fig. 5. Plot of noise-equivalent delta T (NEΔT) for the InSb and HgCdTe detectors, observing a 25 °C blackbody for 1 s. The spectra were calculated when the difference in brightness temperatures between a 25 °C blackbody spectrum and a 25 °C blackbody spectrum with the rms noise subtracted was found.

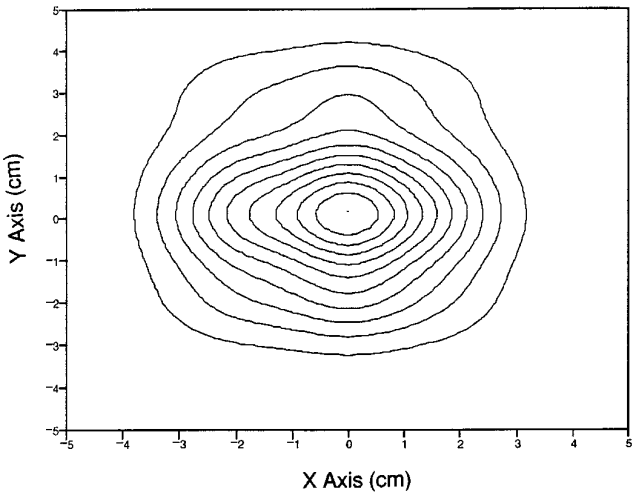

Fig. 6. Plot showing the relative contributions to the IR field of view of the instrument averaged over the 8–14-μm instrument bandpass. This plot was constructed from measurements of the peak-to-peak height of interferograms from a hot soldering iron at a distance of 110 cm, as a function of position relative to the 9-cm diameter of the circular, visible field of view. The background response far outside the field of view was subtracted, and the difference was normalized when it was divided by the response difference in the center of the field of view. The normalized values were divided into ten levels of equal response, shown in the plot. The X axis is parallel to the long side of the instrument enclosure, and the Y axis is parallel to the short side of the instrument enclosure.

the normalized instrument response divided into ten equal intervals. The figure shows that most of the instrument signal exits from within the visible field of view. In practice, the field of view is always overfilled by a factor of 2, if practical, to avoid any possible contamination by off-axis radiance from nontarget material. Samples measured with the $F12$ foreoptics at a distance of 1 m should, then, have a diameter of approximately 16 cm, or 8.0 cm with the use of the $F25$ foreoptics.

D. Calibration Performance

The quality of the calibration was assessed by measurement of the emissivity of the calibration blackbody, the accuracy and linearity of calibration, and the stability of calibration over time. The emissivity of the temperature-controlled blackbody shown in Fig. 7 was calculated from directional hemispheric reflectance measurements to be 0.994–0.998 ± 0.002. Though very close to 1.00, the difference causes an error in the instrument responsivity, calculated to be less than −0.003. A similar error of +0.003 is calculated for the instrument self-emission; both errors are generated because radiance measured from this blackbody is always slightly less than the radiance calculated from a Planck function. Another type of calibration error, caused by the 0.1 °C uncertainty of the blackbody temperature measurement, translates to a fractional error of approximately 0.002.[21] The combined calibration error caused by the blackbody is less than a factor of 0.004.

The calibration linearity was measured to determine optimum blackbody temperatures for the calibration of sample radiances, which depend on the trade-off between measurement precision and instrument linearity. Increasing the temperature difference between warm and cold blackbody sources increases the radiance difference between the measurements without increasing the radiant noise, which reduces the uncertainty of the calculated instrument responsivity and permits more precise calibration. However, the increased precision of calibration is an advantage only to the extent that the instrument response is linear over the range of radiances generated by these blackbody temperatures.

For the calibration linearity to be measured, blackbody radiances were measured between 10 °C and 65 °C at 5° intervals, and the responsivity at 10 and 12 μm was calculated for each 5° interval as a function of blackbody temperature by the use of responsivity Eq. (4). The linear instrument response corresponds to constant responsivity versus temperature. Figure 8 shows point-to-point variations in the responsivity curve, representing uncertainty in the calculations caused by the small temperature interval over which the responsivity was calculated. However, the trend of the measurements suggests that responsivity is relatively constant at 10 and 12 μm for blackbody measurements between 10 °C and 65 °C, which is the normal range of calibration temperatures used for sample surfaces. Thus the selection of widely separated calibration blackbody temperatures should provide greater calibration accuracy than the 5 °C intervals used for the computation of Fig. 8. A temperature interval of 30 °C, for example, should decrease responsivity uncertainty by a factor of 6 compared with the variability shown in Fig. 8. This analysis is confirmed by the accuracy with which intermediate blackbody temperatures and emissivities are retrieved with such calibration (see below).

Although the interpolative calibration error for sources in the 10–65 °C range is negligible for both the InSb and HgCdTe detectors, measurements of the emission from aluminum at a liquid-nitrogen temperature (−196.15 °C), shown in Fig. 9, demonstrate that the extrapolation of room-temperature calibration measurements to low-temperature targets results in a spectral artifact between 11 and 13 μm because of system nonlinearity with the HgCdTe detector. Nonlinearity is indicated by the dependence of the calibrated low-radiance spectra on the blackbody temperatures used in calibration; the artifact worsens as calibration temperatures are

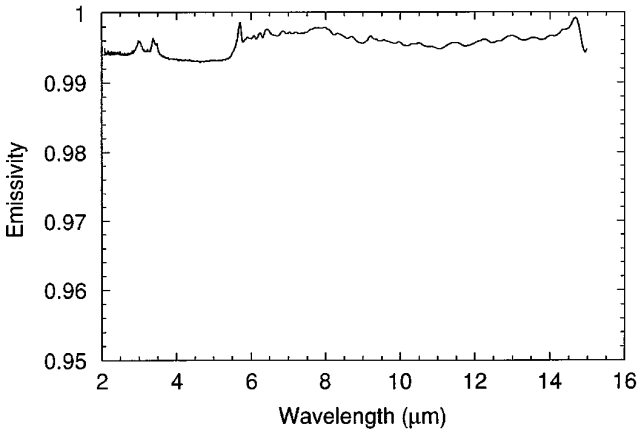

Fig. 7. Blackbody emissivity spectrum calculated from the measurement of DHR.

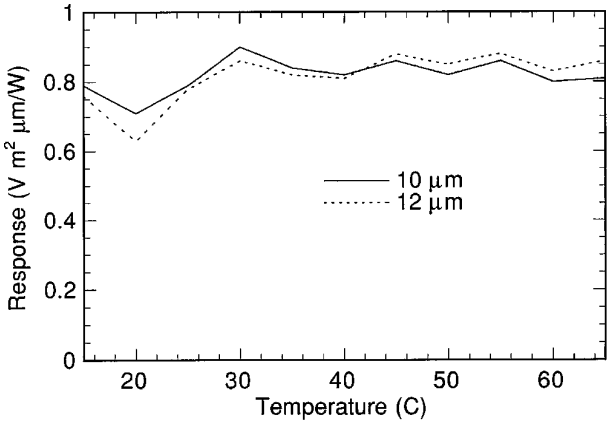

Fig. 8. Instrument responsivity calculation over 5° intervals at 10 and 12 μm, as a function of source brightness temperature. Instrument responsivity was calculated with responsivity Eq. (4).

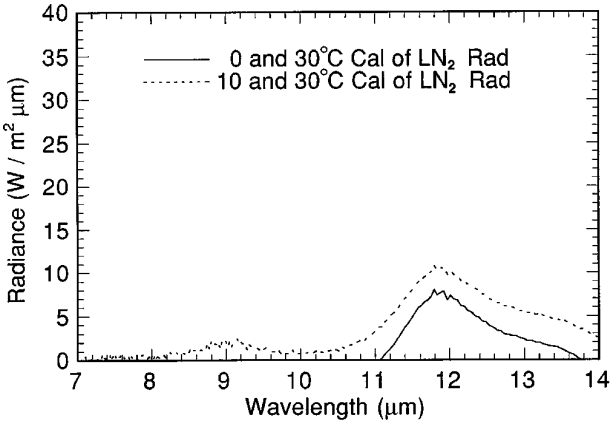

Fig. 9. Radiances from aluminum at liquid-nitrogen (LN_2) temperature calibrated with two different calibration sets.

made further from the target temperature. This effect adds radiance to the spectra between 11 and 13 µm, resulting in a false peak at 11.8 µm. This affects the calibration of DWR's from very clear skies, which have brightness temperatures from 0 to −130 °C, and measured radiances from low-emissivity targets such as polished metals. Radiances from these sources, if calibrated with room-temperature blackbodies, will exhibit the same false peak at 11.8 µm, as the DWR spectra in Fig. 3(a) demonstrate. However, this nonlinearity does not affect the calibration of radiances from most sample surfaces, or DWR's under partly cloudy or humid conditions, as the DWR's spectra in Fig. 3(b) demonstrate. For this range of radiances, with amplitudes between the minimum and maximum blackbody radiances, the calibration procedure interpolates with great accuracy (see the discussion two paragraphs below). In addition, because identical measurements of low-radiance sources collected with the InSb detector were calibrated correctly, independent of calibration temperatures, the instrument may be considered linear in the 3–5-µm region for brightness temperatures between −200 °C and 65 °C. As a result, the calibration for sources in this temperature range will be accurate even with room-temperature calibration.

The low-radiance calibration problem with the HgCdTe detector may be corrected, in principle, by the use of calibration blackbodies that are close to the low-radiance range. However, running a blackbody below the dew-point temperature will cause calibration errors, as water droplets or frost form on the blackbody surface and decrease the blackbody emissivity. A more practical solution minimizes the calibration problem by using the coldest practical blackbody for calibration, as demonstrated in Fig. 9. Two other approaches are being pursued to correct extrapolation error. One can obtain a first-order correction by measuring the emission from liquid-nitrogen-cooled aluminum in addition to the other measurements, calibrating the measurements with the coldest, practical blackbody, and then subtracting the cold aluminum calibrated radiance from the sample radiance. This first-order correction should be a substantial improvement [e.g., subtraction of the upper curve in Fig. 9 from the DWR curve in Fig. 3(a) would result in a substantially correct DWR measurement]. The second approach measures DWR from clear skies with a diffuse reflective panel having a lower reflectance, and thus higher emissivity than the gold panel. During the day the Sun will heat the panel and the panel emission should contribute sufficient radiance to bring the radiance into the linear calibration range. At night the panel will have to be actively heated. In either case, correction for the emission from the panel will become more important to calculate correctly the DWR for subtraction in emissivity derivations.

The stability of calibration over time was measured to assess how frequently calibration measurements should be made. Blackbody radiances at 10 °C and 40 °C measured at the beginning of the experiment were used to calibrate measurements of a 35 °C blackbody made every 5 min over a 60-min period. The 35 °C radiance measurements were used to calculate blackbody emissivity, because emissivity is sensitive to calibration errors and shows how field emissivity spectra will be affected. The blackbody temperatures derived from emissivity calculations were within 0.2 °C of the temperature measured with a platinum resistive thermometer, for all measurements, even 1 h after calibration measurements. Emissivity measurements made in the laboratory remain accurate to within 0.008 for more than 60 min. The calibration for field measurements deteriorates more rapidly because the variable heat load from changing solar insolation typically causes instrument temperature drift. As a result, for maximum accuracy, calibration measurements in the field are repeated with each sample measurement.

E. Precision and Accuracy

Precision and accuracy of the µFTIR were determined in the laboratory as described in the previous paragraph, and both are high. However, such measurements do not answer the question of how well the instrument works in the field, which is a more pertinent question for a field spectrometer. Unfortunately, this answer is strongly governed by variable field conditions, and so does not lend itself to a rigorous statistical approach. As the µFTIR was used under a wide variety of field conditions, one can illustrate the extremes of measurement success by the use of the same samples of quartz sand in different environments. All field measurements shown were made, however, with an earlier pair of detectors that had a lower signal-to-noise ratio than that shown for our current detectors in Fig. 4, particularly at wavelengths longer than 12 µm. Thus, intercomparisons of measurement data in the 8–14-µm atmospheric window are made only from 8 to 12 µm in this section, because they are more representative of the results obtainable throughout the 8–14-µm range with the current detector.

The precision of the instrument in the field can be illustrated by the repeatability of emissivities derived from radiance measurements. Figure 10(a) shows four emissivity spectra of quartz sand measured in a desert environment, each derived from the radiance measurements shown in Fig. 3(a). Figure 10(b) shows similar measurements made under partly cloudy skies in Florida. The partial cloud cover and high humidity noted in the latter measurements greatly increased the error and uncertainty in subtracting DWR in emissivity derivations, because these factors increase both the variability and amount of DWR. Variability in sample emissivities is most intense in the reststrahlen bands where reflectance of DWR is largest. Despite the difficult conditions, the Florida measurements exhibit a standard deviation of only 0.01 between 8 and 12 μm. Under the drier, desert conditions the standard deviation of these measurements is reduced to 0.005 between 8 and 12 μm.

The accuracy of the instrument is illustrated by a comparison of an average of the field-derived emissivities with an emissivity calculated from laboratory measurements of directional hemispherical reflectance (DHR), which should be identical.[21] Under stable, desert atmospheric conditions, such that DWR is relatively constant over time, the average accuracy of emissivity calculations is 0.005 between 8 and 11 μm, as shown in Fig. 11(a). The accuracy between 11 and 12 μm is diminished to 0.02 because the nonlinear instrument response to low-radiance targets in this region causes excess DWR subtraction

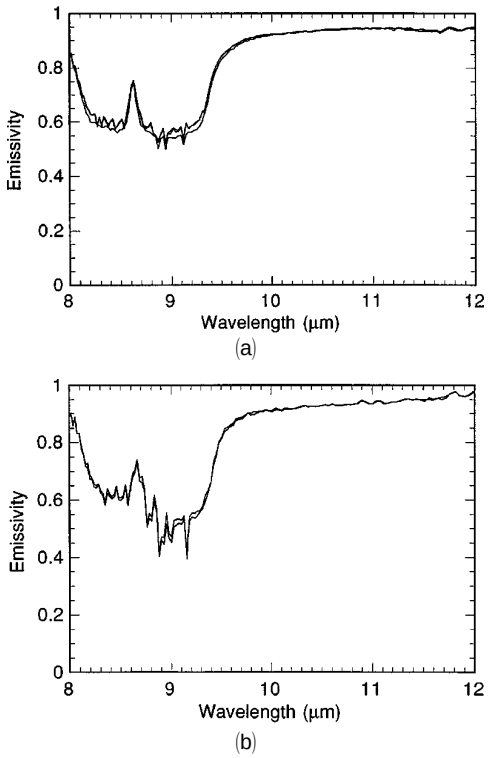

Fig. 10. Four emissivity spectra calculated from the quartz and DWR spectra shown in (a) Fig. 3(a), (b) Fig. 3(b).

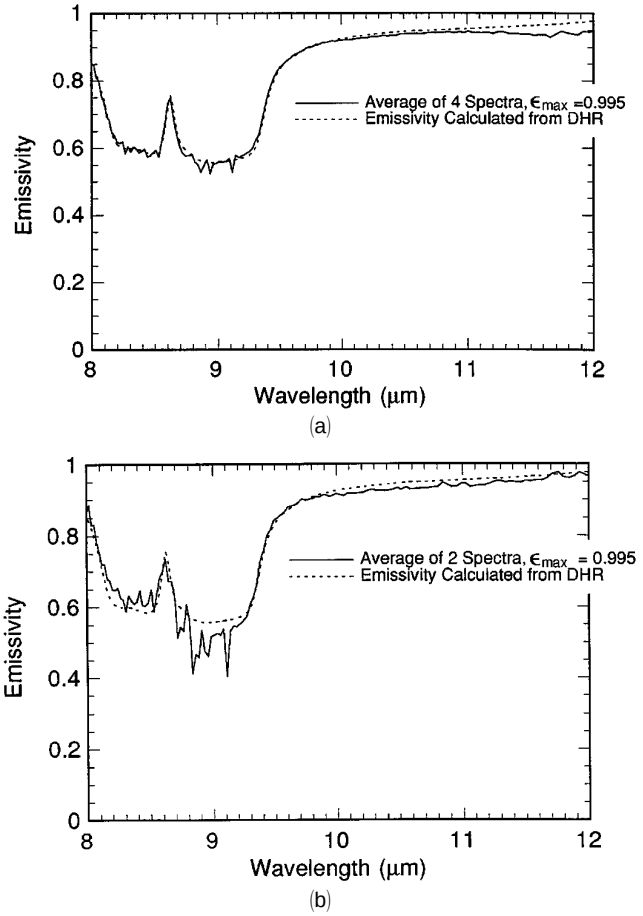

Fig. 11. Comparison of average quartz sand emissivity measured under (a) stable atmospheric conditions with low water vapor content to an emissivity calculated from laboratory measurements of DHR, (b) unstable atmospheric conditions with high water vapor content to an emissivity calculated from laboratory measurements of DHR.

in the emissivity calculation. Obviously, the lower the emissivity and the higher the reflectance of a sample in the 11–13-μm region, the greater this calibration extrapolation error will be. However, this error could be substantially removed by the use of the first-order correction discussed above.

The DWR measured in Florida is not subject to nonlinear response near 12 μm because high humidity and variable cloud cover raise atmospheric emission out of the nonlinear range. However, these factors increase DWR variability with time, which increases the error in subtracting the DWR throughout the spectral region. As a result, the average accuracy of emissivities between 8 and 12 μm is reduced to 0.02 under variable atmospheric conditions, as shown in Fig. 11(b).

Results in the 3–5-μm region are considerably worse than those in the 8–14-μm region under all field conditions. In fact, we find that most of this wavelength region is simply unusable. The problem with this region is threefold. The first problem is that emissions from terrestrial surfaces at temperatures near 30 °C peak near 10 μm and diminish

rapidly as wavelength decreases. Thus, the signal-to-noise ratio for a single scan falls from a peak of ~2700 at 10 μm to 1100 at 5 μm, 500 at 4.5 μm, 205 at 4.0 μm, and only 22 at 3.5 μm. As the signal-to-noise ratio falls, the precision of the measurements falls also.

The second problem is that the 3–5-μm atmospheric window is not as clear as the 8–14-μm window. Strong methane bands between 3.0 and 3.5 μm obscure the short wavelength edge of the window, and the very strong CO_2 band obscures the central 4.0–4.4-μm section of the window. Even the accessible window region with a reasonable signal-to-noise ratio between 4.4 and 5.0 μm contains atmospheric water vapor features and continuum absorption. The presence of these spectral features portends rapid DWR variation with time as water vapor distribution varies. Most important, the emissivities of both natural and man-made materials tend to be relatively low in this region of the spectrum. As a result, reflected DWR is a larger fraction of measured sample radiance. Thus rapid changes in DWR cause lower precision and accuracy in the 3–5-μm region than in the 8–14-μm region, as the comparison of average field emissivity with emissivity calculated from laboratory measurements of DHR reflectance illustrates in Fig. 12. These measurements, made under stable atmospheric conditions at high altitude with very low atmospheric water vapor content, have an accuracy of 0.04 between 4.5 and 4.9 μm.

The variability of DWR on a time scale shorter than the time between sample and DWR measurements is the principal source of the errors seen above, and it is much greater than the fractional error contributed by calibration (~0.004) and the temperature estimation of a sample with known emissivity (~0.002). Even if DWR is constant, however, its subtraction introduces an uncertainty to emissivity calculations that depends on the magnitude of the difference between the sample radiance and the DWR. Subtraction of the DWR reduces the sample signal without decreasing the noise level. As a result, the emissivity spectrum is always noisier than the radiance spectrum. In the worst case, i.e., a laboratory measurement of a sample in thermal equilibrium with the ceiling and walls, or a field measurement in low overcast conditions, the sample radiance and DWR are equal Planck functions, and calculations derive a noisy emissivity of one (the algorithm blows up). This phenomenon also results in added noise near the margins of atmospheric windows, where atmospheric emission may approach sample emission (compare Figs. 3 and 11). Thus, under high humidity conditions with a warm atmosphere, the portion of the atmospheric window beyond ~13 μm may be inaccessible [see Fig. 11(b)], although the better signal-to-noise ratio of the two-element detector is expected to minimize this effect.

F. Instrument Durability in Field Campaigns

The durability of the instrument in the field was tested during measurements over 3 yr in conditions ranging from a cold (5 °C) mountaintop at 4328 m (14,200 ft) elevation to a hot and muggy (100% relative humidity at 40 °C) swamp, collecting data mounted on tripods, cherrypickers, a step ladder, and a hot-air balloon. Sensitivity to vibration was tested by the recording of data from a helicopter and from a van driving down a rough dirt road at 56 kph (35 mph). Measurements of the emission from a short air path, shown in Fig. 13, in the moving van show little degradation of spectral features compared with the equivalent stationary measurement. The instrument has also survived a 6-ft (~1.8-m) fall, a dust storm, overhead luggage compartment travel, and postal shipment without loss of alignment. Without repairs or optical alignment over 3 yr, the μFTIR instrument signal-to-noise ratio degraded by less than 10%.

G. Future Instrument Improvements

The most important instrument improvement will reduce the error of extracting DWR for emissivity

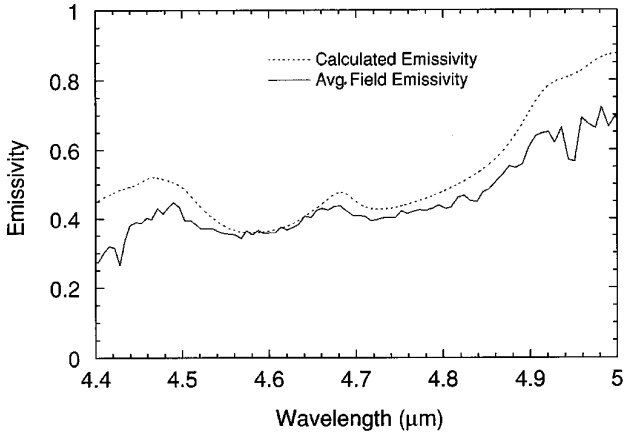

Fig. 12. Average emissivity calculated from four measurements of fine (<75 μm) quartz powder, compared with an emissivity calculated from laboratory measurements of DHR.

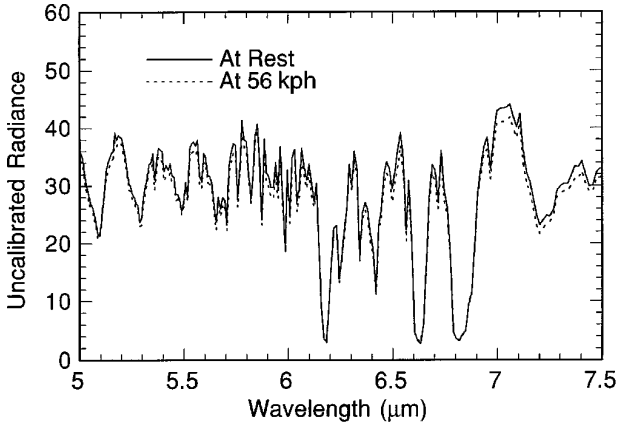

Fig. 13. Measurements of emission from an air path at ambient temperature by the μFTIR mounted in a van driving down a dirt road at 56 kph, compared with a stationary measurement.

calculations by reducing the time between the sample and DWR measurement. This will be accomplished by having a split field of view that observes the sample and DWR simultaneously, or by measuring sample and DWR in alternate scans.

The resolution of the instrument could be made into a switchable option to allow lower (6 cm^{-1}) spectral resolution (which produces measurements with higher signal-to-noise ratios) for emissivity measurements, and higher spectral resolution (1 cm^{-1}), with a lower signal-to-noise ratio, for atmospheric measurements.

The instrument could be improved by automating tasks, or by allowing the user to program tasks such as calibration measurements, multiple measurements of several samples and DWR, scan initiation, and recording spectra into data files.

The liquid-nitrogen-cooled Dewar could be replaced with Sterling coolers for operation in areas in which liquid nitrogen is difficult to obtain. The instrument could also be improved to allow simultaneous measurements with both the InSb and HgCdTe detectors. Currently, data are collected from only one detector at a time, although the use of a two-element detector permits rapid switching of wavelength ranges. Ultimately, the two-element detector could also be replaced with a multipixel detector to produce an ultraspectral image cube.

5. Conclusions

The μFTIR instrument is a hand-portable, battery-powered spectroradiometer that measures radiances in the 3–5-μm and 8–14-μm atmospheric windows. Emissivities derived from radiance measurements made in the field have an accuracy of 0.04 in accessible regions of the 3–5-μm window, and of 0.02 (or better) in the 8–14-μm atmospheric window. The combination of accuracy, hand portability, and durability of the instrument enables measurement programs to study emission behavior in the field, to examine the effects of atmospheric conditions, to measure the agreement between laboratory and field measurements of emissivity, and to support satellite and airborne infrared measurements with ground-truth programs.

The assistance of D. Hetzel, G. M. Cushman, D. D'Aria, and E. P. Moore in generating the figures and data is gratefully acknowledged.

References

1. S. Hook and A. B. Kahle, "μFTIR—a new field spectrometer for validation of infrared data," Remote Sensing Environ. (to be published).
2. *M21—remote sensing chemical agent alarm (RSCAAL)* (Brunswick Defense, Deland, Fla., 1992), pp. 1–24.
3. J. C. Brasunas, V. G. Kunde, and L. W. Herath, "Cryogenic Fourier spectrometer for measuring trace species in the lower stratosphere," Appl. Opt. **27,** 4964–4976 (1988).
4. R. C. Carlson, A. F. Hayden, and W. B. Telfair, "Remote observations of effluents from small building smokestacks using FTIR spectroscopy," Appl. Opt. **27,** 4952–4959 (1988).
5. L. C. Block and A. S. Zachor, "Inflight satellite measurements of infrared spectral radiance of the Earth," Appl. Opt. **3,** 209–214 (1964).
6. R. A. Hanel, B. Schlachman, F. D. Clark, C. H. Prokesh, J. B. Taylor, W. M. Wilson, and L. Chaney, "The Nimbus III Michelson interferometer," Appl. Opt. **9,** 1767–1774 (1970).
7. R. A. Hanel, D. Crosby, L. Herath, D. Vanous, D. Collins, H. Creswick, C. Harris, and D. Rhodes, "Infrared spectrometer for Voyager," Appl. Opt. **19,** 1391–1400 (1980).
8. J. W. Salisbury, "First use of a new portable thermal infrared spectrometer," in *Proceedings of the Tenth Annual IEEE International Geoscience and Remote Sensing Symposium* (Institute of Electrical and Electronics Engineers, New York, 1990), pp. 1775–1778.
9. F. M. Luther, R. G. Ellingson, Y. Fouquart, S. Fels, N. A. Scott, and W. J. Wiscombe, "Intercomparison of radiation codes in climate models (ICRCCM): longwave clear-sky results—a workshop summary," Am. Meterol. Soc. Bull. **69,** 40–48 (1988).
10. S. A. Ackerman, W. L. Smith, J. D. Spinhirne, and H. E. Revercomb, "The 27–28 October 1986 FIRE IFO cirrus case study: spectral properties of cirrus clouds in the 8–12 μm window," Mon. Weather Rev. **118,** 2377–2388 (1990).
11. D. Lubin, "The role of the tropical super greenhouse effect in heating the ocean surface," Science **265,** 224–227 (1994).
12. R. J. Bell, *Introductory Fourier Transfer Spectroscopy* (Academic, New York, 1972), Chap. 1.
13. H. E. Revercomb, H. Buijs, H. B. Howell, D. D. LaPorte, W. L. Smith, and L. A. Sromovsky, "Radiometric calibration of IR Fourier transform spectrometers: solution to a problem with the high-resolution interferometer sounder," Appl. Opt. **27,** 3210–3218 (1988).
14. H. L. Buijs, "A class of high resolution ruggedized Fourier transform spectrometers," in *Multiple and/or High Throughput Spectroscopy,* G. A. Vanasse, ed., Proc. Soc. Photo-Opt. Instrum. Eng. **191,** 116 (1979).
15. H. L. Buijs, D. J. W. Kendall, G. Vail, and J. N. Berube, "Fourier transform infrared hardware developments," in *1981 International Conference on Fourier Transform Infrared Spectroscopy,* H. Sakai, ed., Proc. Soc. Photo-Opt. Instrum. Eng. **289,** 322 (1981).
16. *Bomem FT-IR Spectroradiometer Catalog,* (Bomen, Inc., Québec, Canada, 1993), p. 29.
17. H. E. Revercomb, H. Buijs, H. B. Howell, R. O. Knuteson, D. D. LaPorte, W. L. Smith, L. A. Sromovsky, and H. W. Wolf, "Radiometric calibration of IR interferometers: experience from the high-resolution interferometer sounder (HIS) aircraft instrument," in *RSRM 87: Advances in Remote Sensing Retrieval Methods,* A. Deepak, H. E. Fleming, and J. S. Theon, eds., (Deepak Publishing, Hampton, Va., 1989), pp. 89–102.
18. J. W. Salisbury and D. M. D'Aria, "Emissivity of terrestrial materials in the 8–14 μm atmospheric window," Remote Sensing Environ. **42,** 83–106 (1992).
19. A. B. Kahle and R. E. Alley, "Separation of temperature and emittance in remotely sensed radiance measurements," Remote Sensing Environ. **42,** 107–111 (1992).
20. J. W. Salisbury and D. M. D'Aria, "Emissivity of terrestrial materials in the 3–5 μm atmospheric window," Remote Sensing Environ. **47,** 345–361 (1994).
21. J. W. Salisbury, A. E. Wald, D. M. D'Aria, "Thermal-infrared remote sensing and Kirchhoff's law 1. Laboratory measurements," J. Geophys. Res. **99,** 11,897–11,911 (1994).